The Effects of Spiral Anisotropy on the Electric Potential and the Magnetic Field at the Apex of the Heart*

BRADLEY J. ROTH, WEI-QIANG GUO,

AND

JOHN P. WIKSWO, JR.

Living State Physics Group, Department of Physics and Astronomy, Vanderbilt University, Nashville, Tennessee 37235

Received 9 January 1987; revised 27 October 1987

ABSTRACT

This paper describes a volume-conductor model of the apex of the heart that accounts for the spiraling tissue geometry. Analytic expressions are derived for the potential and magnetic field produced by a cardiac action potential propagating outward from the apex. The model predicts the existence of new information in the magnetic field that is not present in the electrical potential.

INTRODUCTION

A central question in biomagnetism is whether a biomagnetic field can contain information not present in the bioelectric potential. We will address this question by calculating the electric and magnetic fields produced at the apex of the heart. Figure 1 shows one of the unique features of this tissue: the unusual geometry of the fibers, which spiral around a central vortex at the apex of the left ventricle. Our goal is to calculate the electric and magnetic fields produced by a propagating cardiac action potential using a model of the apex of the heart that incorporates this spiraling structure. In particular, we will show that this fiber geometry leads to biomagnetic fields that contain information about the tissue that cannot be obtained from the bioelectric potential. Such "electrically silent magnetic fields" can be produced in tissues with either spiraling or helical fiber geometries [1]. At the apex of the heart, these electrically silent magnetic fields are exceptionally

*Address reprint requests to John P. Wikswo, Jr., Department of Physics and Astronomy, Vanderbilt University, Box 1807, Station B, Nashville, TN 37235.

52 Vanderbilt Ave., New York, NY 10017 0025-5564/88/$03.50

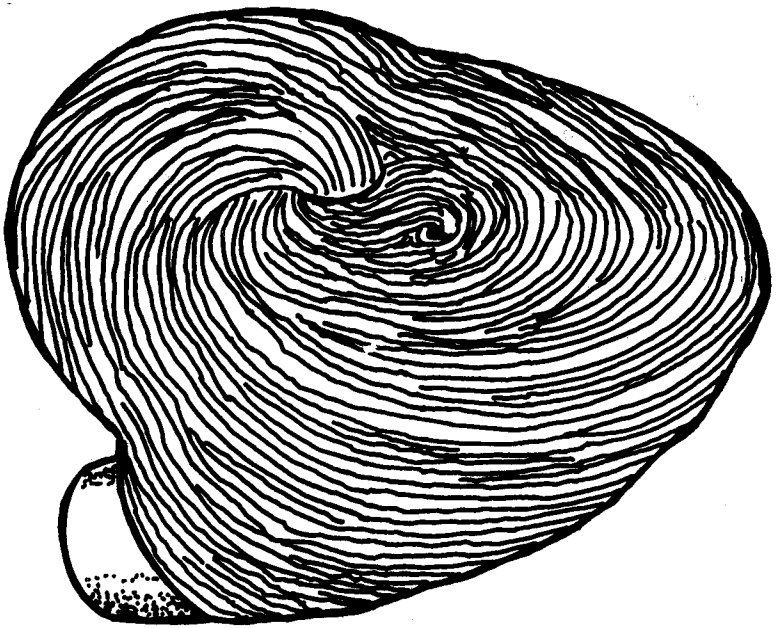

FIG. 1. A drawing of the apex of the heart. Taken from an anatomical study by Mall, 1911 [48].

large, and should be easily detectable in an experiment using a SQUID magnetometer.

INFORMATION CONTENT OF THE MCG

Since the first measurement of the magnetocardiogram by Baule and Mcfee in 1963 [2], there has been a question whether the magnetocardiogram (MCG) contains information not present in the electrocardiogram (ECG). It is possible to postulate simple current sources representing the cardiac electrical activity that have identical electric potentials at the body surface, but have different magnetic fields [3]. Any impressed current density in the heart can be represented by a Helmholtz decomposition, and in 1972 Plonsey used this fact to show that the ECG and MCG might contain independent information [4]. Rush subsequently argued that physiological constraints prevent the ECG and the MCG from having different information content [5]. Wikswo and Barach suggested a counterexample to Rush's arguments in which two impressed current distributions in the heart have identical external electric fields but differing external magnetic fields [6]. The physiological motivation for Wikswo and Barach's prediction was the observation by Corbin and Scher that the anisotropy of cardiac tissue could

produce current distributions, associated with small, spherical or hemispherical wavefronts, that were not consistent with the then widely accepted uniform double-layer model of cardiac activation [7]. The work by Corbin and Scher has since been confirmed and extended by several authors [8–11]. Using a multipole expansion of the impressed current source, Katila and Karp [12] and Wikswo [13] have shown that the antisymmetric part of the impressed-current quadrupole tensor produces new information in the MCG. However, in 1982 Plonsey suggested that measurements of the external bioelectric field do, in fact, completely determine the external biomagnetic field because the impressed current contributes much less to the biomagnetic fields than do secondary sources due to the presence of the resistive cell membranes [14]. The general relationship between the ECG and MCG, and the possibility that the magnetic field of the heart might contain information not present in the electric potential, were reviewed by Wikswo [13].

There have been several recent theoretical investigations into the relative information content of bioelectric and biomagnetic fields. Titomir and Kneppo [15, 16] have shown how multipole expansions of the cardiac electric and magnetic fields can be used to detect new information. Using a bidomain model of cardiac tissue, Sepulveda and Wikswo [17] demonstrated that measurements of the electric action potential alone are insufficient to completely determine the electrical properties of cardiac muscle, but that combined measurements of the magnetic and electric fields can be used to determine these properties. Roth and Wikswo [1] have shown that bioelectric potentials produced in tissues with spiraling or helical fiber geometries can lead to electrically silent magnetic fields, and they derived analytic equations for these fields in the special case of a cylindrical strand of fibers. The unusual fiber geometry was incorporated into their model by including off-diagonal terms in the conductivity tensor.

Only recently has experimental evidence been obtained to address the question of information content of the MCG. Burstein and Cohen [18] found that one-dimensional strands of frog cardiac muscle generate magnetic and electric fields that contain the same information when measured from 1 to 5 cm away from a wavefront 1 mm or less long propagating along the strand. However, these experiments do not exclude the possibility that electrically silent magnetic fields might be produced in tissues with more complex fiber geometries. On the other hand, recordings of the magnetocardiogram by MacAulay et al. [19,20], Nousiainen et al. [21], Varpula et al. [22], and Gonnelli and Agnello [23] provide evidence that there may be new information in the MCG.

Preliminary comparisons of experimental MCG maps with calculations of the heart's magnetic field that take into account the anisotropy of cardiac tissue are just beginning to appear. Campos et al. [24] have calculated the MCG using a multiple dipole model and Durrer et al.'s [25] data for

propagation of the cardiac wavefront in the normal heart. They accounted for the tissue anisotropy by orienting the dipoles at an angle with respect to the direction of propagation, and found that their model could predict many of the features observed in experimentally measured MCGs. Gonnelli and Agnello [26] have similarly modeled the cardiac activation wavefront as a hemisphere, using Streeter's [27] data for the fiber orientation in the heart. Their calculated MCG maps also showed a striking resemblance to measured data.

METHODS

Many of the previous theoretical and experimental studies of the MCG suffer from the lack of accurate knowledge of the exact shape of the heart, the fiber geometry, and the precise path of the depolarization wavefront. It seems that a better way to answer the fundamental question of information content is to study as simple a system as possible, but one that is still complex enough to produce electrically silent magnetic fields. A small circular wavefront initiated at the apex of the heart is such a system.

Our calculation does not predict MCG maps, as does the work of Campos et al. [24] and Gonnelli and Agnello [26]. However, our model does have several advantages over these other works. First, the system is idealized enough that a fairly simple analytic solution can be found for both the electric potential and the magnetic field, allowing us to answer unambiguously questions about the relative information content of these two fields. Second, the model can be tested by an *in vitro* experiment, allowing the experimenter to have much more control over the experimental parameters and conditions. Idealized models and *in vitro* experiments are always open to the criticism that they are artificial and do not accurately represent the properties of the whole heart *in vivo*. However, these criticisms must be weighed against the extreme difficulty of developing models of the whole heart, with all its complexity, and especially the uncertainties in validating these models experimentally. This calculation is not meant to quantitatively model the whole heart *in vivo*. It does model a possible *in vitro* experiment, and may provide some insight into the qualitative interpretation of the MCG.

We will ignore the overall curvature of the heart and assume that the apex is essentially a plane slab of tissue of thickness l (see Figure 2). This will be a good approximation as long as the distance from the apex to the depolarization wavefront is small compared to the radius of curvature of the heart. The tissue is assumed to lie in an unbounded saline bath with conductivity σ_e. We consider only action potentials that originate at the apex and propagate radially outward. This is a good approximation to an *in vitro* experiment in which the tissue is stimulated at the apex. We use a cylindrical

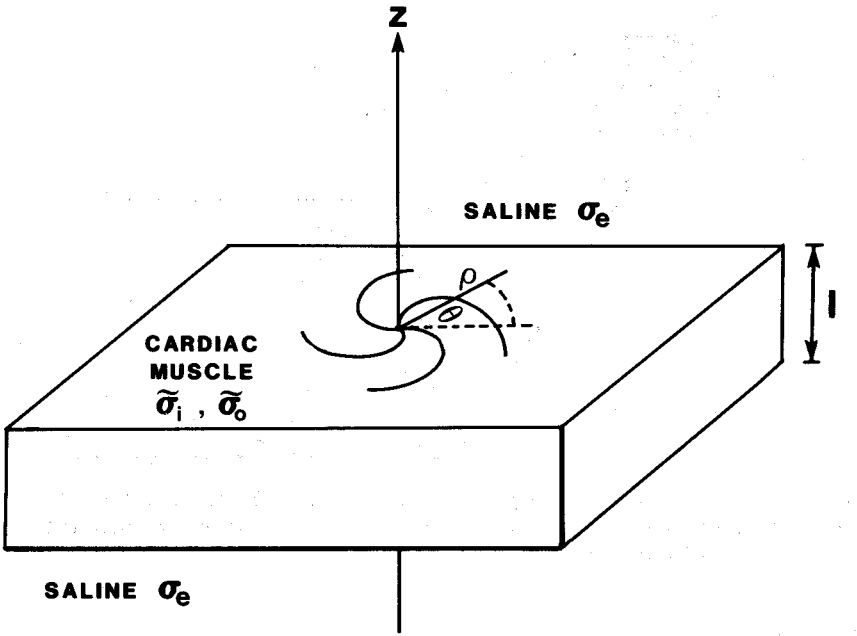

FIG. 2. The geometry of a slab of cardiac tissue. The thickness of the tissue is l, the conductivity of the saline bath is σ_e, and the conductivities of the intracellular and interstitial volumes of the tissue are $\tilde{\sigma}_i$ and $\tilde{\sigma}_o$ respectively. The variables ρ and θ are the cylindrical coordinates, and the curved lines represent the local fiber direction.

coordinate system to describe the tissue, with the z-axis passing through the apex center, oriented perpendicular to the plane of the tissue. The variables ρ and θ are the radial and azimuthal coordinates, shown in Figure 2. We assume that the tissue is cylindrically symmetric, which amounts to ignoring the presence of the second vortex in Figure 1 due to the right ventricle. This is valid if we assume that the wavefront has not moved beyond the left ventricle.

Cardiac tissue is a syncytium, and therefore can be represented by a bidomain model [28–32], with intracellular and interstitial conductivity tensors $\tilde{\sigma}_i$ and $\tilde{\sigma}_o$, respectively. The components of the conductivity tensors are determined by the electrical properties of the tissue and the fiber geometry. On a large scale (millimeters) the fiber direction changes with position as the fibers spiral around the apex. We assume, however, that on a smaller scale (tenths of millimeters) each patch of tissue has a well-defined local fiber direction (Figure 3). In principle this direction of highest conductivity could be different in the intracellular and interstitial domains, although in practice this is unlikely; however, the anisotropy ratios in the two spaces are most likely different [33]. Let us assume that for the intracellular

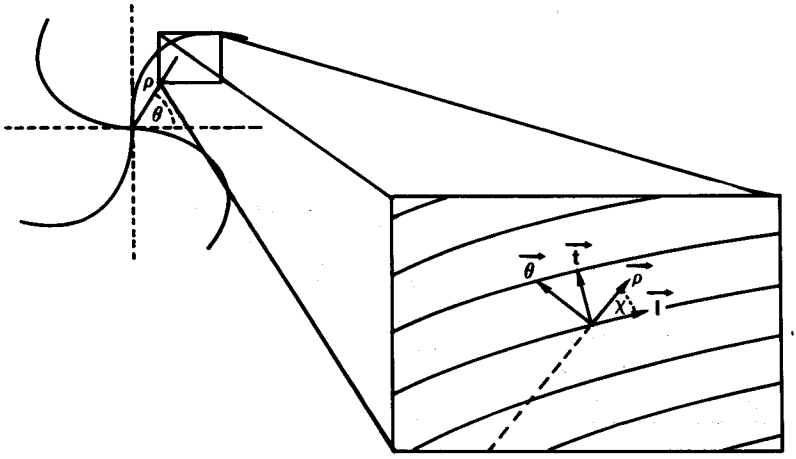

FIG. 3. The unit vectors **l** and **t** represent the directions parallel and perpendicular to the local fiber direction. The vectors **ρ** and **θ** are the unit vectors in the cylindrical coordinate system. The angle between **l** and **ρ** is χ.

domain the direction parallel to the local fiber direction, termed the longitudinal direction, has conductivity σ_{il}, and the direction perpendicular to the local fiber direction, termed the transverse direction, has conductivity σ_{it}, and that σ_{il} and σ_{it} are constant throughout the tissue. Furthermore, we assume that the longitudinal direction makes everywhere a constant angle χ_i with the **ρ**-direction (Fig. 3). Then for any small region of tissue, the intracellular conductivity tensor can be written with respect to a local coordinate system oriented along the longitudinal direction as

$$\begin{pmatrix} \sigma_{il} & 0 & 0 \\ 0 & \sigma_{it} & 0 \\ 0 & 0 & \sigma_{it} \end{pmatrix}. \tag{1}$$

To represent this tensor in cylindrical coordinates, we must rotate our frame of reference from one aligned with the fiber direction to one oriented along the **ρ**, **θ**, and **z** directions. To rotate a tensor, we must multiply it on each side by a rotation matrix

$$\begin{pmatrix} \sigma_i^{\rho\rho} & \sigma_i^{\theta\rho} & 0 \\ \sigma_i^{\theta\rho} & \sigma_i^{\theta\theta} & 0 \\ 0 & 0 & \sigma_i^{zz} \end{pmatrix}$$

$$= \begin{pmatrix} \cos\chi_i & \sin\chi_i & 0 \\ -\sin\chi_i & \cos\chi_i & 0 \\ 0 & 0 & 1 \end{pmatrix} \begin{pmatrix} \sigma_{il} & 0 & 0 \\ 0 & \sigma_{it} & 0 \\ 0 & 0 & \sigma_{it} \end{pmatrix} \begin{pmatrix} \cos\chi_i & -\sin\chi_i & 0 \\ \sin\chi_i & \cos\chi_i & 0 \\ 0 & 0 & 1 \end{pmatrix}, \tag{2}$$

which leads to

$$\begin{pmatrix} \sigma_i^{\rho\rho} & \sigma_i^{\theta\rho} & 0 \\ \sigma_i^{\theta\rho} & \sigma_i^{\theta\theta} & 0 \\ 0 & 0 & \sigma_i^{zz} \end{pmatrix}$$

$$= \begin{pmatrix} \sigma_{il}\cos^2\chi_i + \sigma_{it}\sin^2\chi_i & -(\sigma_{il}-\sigma_{it})\cos\chi_i\sin\chi_i & 0 \\ -(\sigma_{il}-\sigma_{it})\cos\chi_i\sin\chi_i & \sigma_{il}\sin^2\chi_i + \sigma_{it}\cos^2\chi_i & 0 \\ 0 & 0 & \sigma_{it} \end{pmatrix}. \quad (3)$$

The conductivity tensor has four independent nonvanishing components: the three diagonal components $\sigma_i^{\rho\rho}$, $\sigma_i^{\theta\theta}$, and σ_i^{zz}, and one off-diagonal component $\sigma_i^{\theta\rho}$. The off-diagonal one reflects the spiraling tissue geometry. The assumption that the angle χ_i is constant throughout the tissue implies that the conductivity tensor is independent of position.

If $\chi_i = 0$ or 90°, the off-diagonal components vanish, and if $\chi_i = 45°$, they have their maximum value. When the angle χ_i is 45°, the conductivity tensor has the simple form

$$\begin{pmatrix} \sigma_i^{\rho\rho} & \sigma_i^{\theta\rho} & 0 \\ \sigma_i^{\theta\rho} & \sigma_i^{\theta\theta} & 0 \\ 0 & 0 & \sigma_i^{zz} \end{pmatrix} = \begin{pmatrix} \frac{\sigma_{il}+\sigma_{it}}{2} & -\frac{\sigma_{il}-\sigma_{it}}{2} & 0 \\ -\frac{\sigma_{il}\sigma_{it}}{2} & \frac{\sigma_{il}+\sigma_{it}}{2} & 0 \\ 0 & 0 & \sigma_{it} \end{pmatrix}. \quad (4)$$

Furthermore, if the longitudinal conductivity is much greater than the transverse conductivity, then the conductivity tensor has the even simpler form

$$\begin{pmatrix} \sigma_i^{\rho\rho} & \sigma_i^{\theta\rho} & 0 \\ \sigma_i^{\theta\rho} & \sigma_i^{\theta\theta} & 0 \\ 0 & 0 & \sigma_i^{zz} \end{pmatrix} \approx \begin{pmatrix} \sigma_{il}/2 & -\sigma_{il}/2 & 0 \\ -\sigma_{il}/2 & \sigma_{il}/2 & 0 \\ 0 & 0 & \sigma_{it} \end{pmatrix}. \quad (5)$$

In this case, the off-diagonal terms are as large as the diagonal terms.

In a similar way the interstitial conductivity tensor $\tilde{\sigma}_o$ can be evaluated from the interstitial longitudinal (σ_{ol}) and transverse (σ_{ot}) conductivities, and the angle χ_o between ρ and the interstitial fiber direction. For the remainder of this paper, we will only consider the case in which the intracellular and interstitial domains have the same longitudinal direction, i.e. $\chi_i = \chi_o = \chi$.

Once the conductivity tensors describing the tissue are known, we can calculate the volume conducted electric potential and current. The fundamental equations governing the electric potential are the equation of con-

tinuity of current

$$\nabla \cdot (\mathbf{J}_o + \mathbf{J}_i) = 0, \qquad -l/2 < z < l/2 \tag{6}$$

$$\nabla \cdot \mathbf{J}_e = 0, \qquad |z| > l/2, \tag{7}$$

and Ohm's law

$$\mathbf{J}_i = \tilde{\sigma}_i \mathbf{E}_i, \tag{8}$$

$$\mathbf{J}_o = \tilde{\sigma}_o \mathbf{E}_o, \tag{9}$$

$$\mathbf{J}_e = \sigma_e \mathbf{E}_e, \tag{10}$$

where $\mathbf{E}$ represents the electric field, $\mathbf{J}$ the current density, and the subscripts i, o, and e signify the intracellular, interstitial, and external bath volumes. These equations can be combined with the definition of the electric field in terms of the potential,

$$\mathbf{E} = -\nabla \Phi, \tag{11}$$

the assumption of cylindrical symmetry, and the assumption that the conductivity tensors are independent of position to yield two partial differential equations describing the intracellular, interstitial, and external potentials Φ_i, Φ_o, and Φ_e:

$$\frac{1}{\rho}\frac{\partial}{\partial \rho}\left[\rho \frac{\partial}{\partial \rho}\left(\sigma_i^{\rho\rho}\Phi_i + \sigma_o^{\rho\rho}\Phi_o\right)\right] + \frac{\partial^2}{\partial z^2}\left(\sigma_i^{zz}\Phi_i + \sigma_o^{zz}\Phi_o\right) = 0, \qquad -\frac{l}{2} < z < \frac{l}{2}, \tag{12}$$

$$\nabla^2 \Phi_e = 0, \qquad |z| > \frac{l}{2}. \tag{13}$$

The boundary conditions at the surface of the tissue, $|z| = l/2$, are [32]

$$J_o^z + J_i^z = J_e^z, \tag{14}$$

and

$$\Phi_o = \Phi_e. \tag{15}$$

Equation (12) is quite complicated, but can be made tractable using a few algebraic manipulations. Following the technique given in [32], we make a change of variable

$$z^* = \lambda z, \tag{16}$$

where

$$\lambda = \sqrt{\frac{\sigma_i^{\rho\rho} + \sigma_o^{\rho\rho}}{\sigma_i^{zz} + \sigma_o^{zz}}}, \tag{17}$$

and introduce two new potentials Ψ and Φ_m, which are linear combinations of Φ_i and Φ_o:

$$\Phi_m(\rho) = \Phi_i(z,\rho) - \Phi_o(z,\rho), \tag{18}$$

$$\Psi(z,\rho) = \Phi_i(z,\rho) + \frac{\sigma_o^{\rho\rho}}{\sigma_i^{\rho\rho}}\Phi_o(z,\rho). \tag{19}$$

Equation (18) is the usual definition of the transmembrane potential, which we assume is known. Note that Φ_m is assumed to be a function only of ρ, consistent with our assumption of radial propagation of the action potential. Equation (19) defines Ψ. We can invert the above two equations to obtain

$$\Phi_o(z,\rho) = \frac{\sigma_i^{\rho\rho}}{\sigma_i^{\rho\rho} + \sigma_o^{\rho\rho}}\left[\Psi(z,\rho) - \Phi_m(\rho)\right], \tag{20}$$

$$\Phi_i(z,\rho) = \frac{\sigma_i^{\rho\rho}}{\sigma_i^{\rho\rho} + \sigma_o^{\rho\rho}}\left[\Psi(z,\rho) + \frac{\sigma_o^{\rho\rho}}{\sigma_i^{\rho\rho}}\Phi_m(\rho)\right]. \tag{21}$$

Making these substitutions into Equation (12), and using the fact that Φ_m is independent of z, we find that

$$\nabla^{*2}\Psi(z^*,\rho) = 0, \qquad -l/2 < z < l/2, \tag{22}$$

which is Laplace's equation in the (z^*,ρ) coordinate system. The boundary conditions of Equations (14) and (15) become

$$\frac{\partial\Psi}{\partial z} = \lambda^2\frac{\sigma_e}{\sigma_i^{\rho\rho}}\frac{\partial\Phi_e}{\partial z} \tag{23}$$

and

$$\Psi = \Phi_m + \frac{\sigma_i^{\rho\rho} + \sigma_o^{\rho\rho}}{\sigma_i^{\rho\rho}}\Phi_e. \tag{24}$$

Our problem is now reduced to solving Laplace's equation [Equations (13) and (22)] with the appropriate boundary conditions [Equations (23) and (24)]. Therefore, if we are given the tissue parameters and the transmembrane potential as a function of ρ, we can derive analytic expressions for the potentials in the intracellular, interstitial, and external volumes. This derivation is outlined in Appendix A.

The most significant result of this calculation is that $\sigma_i^{\theta\rho}$ *and* $\sigma_o^{\theta\rho}$ *do not appear in any of the equations governing the intracellular, interstitial, or external potentials.* The electric potential is independent of the off-diagonal conductivity terms, so it is not affected by the spiraling geometry of the

tissue. However, $\sigma_i^{\theta\rho}$ *and* $\sigma_o^{\theta\rho}$ *do appear in the expressions for the current density*,

$$\mathbf{J}_i = -\sigma_i^{\rho\rho}\frac{\partial\Phi_i}{\partial\rho}\boldsymbol{\rho} - \sigma_i^{\theta\rho}\frac{\partial\Phi_i}{\partial\rho}\boldsymbol{\theta} - \sigma_i^{zz}\frac{\partial\Phi_i}{\partial z}\mathbf{z}, \tag{25}$$

$$\mathbf{J}_o = -\sigma_o^{\rho\rho}\frac{\partial\Phi_o}{\partial\rho}\boldsymbol{\rho} - \sigma_0^{\theta\rho}\frac{\partial\Phi_o}{\partial\rho}\boldsymbol{\theta} - \sigma_o^{zz}\frac{\partial\Phi_o}{\partial z}\mathbf{z}, \tag{26}$$

$$\mathbf{J}_e = -\sigma_e\frac{\partial\Phi_e}{\partial\rho}\boldsymbol{\rho} - \sigma_e\frac{\partial\Phi_e}{\partial z}\mathbf{z}. \tag{27}$$

Thus, there are currents circling around the apex in the θ-direction, although there are no potential gradients in that direction. This result is due entirely to the spiral geometry of the fibers, expressed mathematically by the off-diagonal terms in the conductivity tensors, and leads directly to the production of electrically silent magnetic fields [1].

The law of Biot and Savart governs the behavior of the magnetic field. This equation can be solved analytically for the magnetic field **B** produced at the apex of the heart in terms of the transmembrane potential, as is done in Appendix B. The result shows that there are components of the magnetic field in all three directions, and that the ρ and z components both depend on $\sigma_i^{\theta\rho}$ and $\sigma_o^{\theta\rho}$. Thus, *the off-diagonal components of the conductivity tensor appear in the expressions for the magnetic field, but do not appear in the expressions for the electrical potential.* We term the ρ and z components of the magnetic field the *electrically silent components*; they contain new information that is not present in the electric potential.

RESULTS

To calculate the potential and magnetic field from the expressions in Appendices A and B, we must assign specific values to the parameters describing the cardiac tissue and action potential. We use a parametrization based on Plonsey and Barr's representation of the transmembrane potential [33]

$$\Phi_m(\rho) = \frac{V_{pk}}{2}\left[1 + \tanh\left(\frac{2\dot{V}_{\max}}{uV_{\mathrm{pk}}}(\rho_0 - \rho)\right)\right], \tag{28}$$

shown in Figure 4, where V_{pk} is the amplitude of the action potential (110 mV), $\dot{V}_{\max}$ is its maximum rate of rise (200 V/s), and u is its propagation velocity (0.30 m/s) [34]. This transmembrane potential represents a circular activation wavefront propagating radially outward from the apex of the heart, as if a stimulating electrode had been placed at the vortex. The wavefront will have a radius ρ_0, and a width (10 to 90% of maximum)

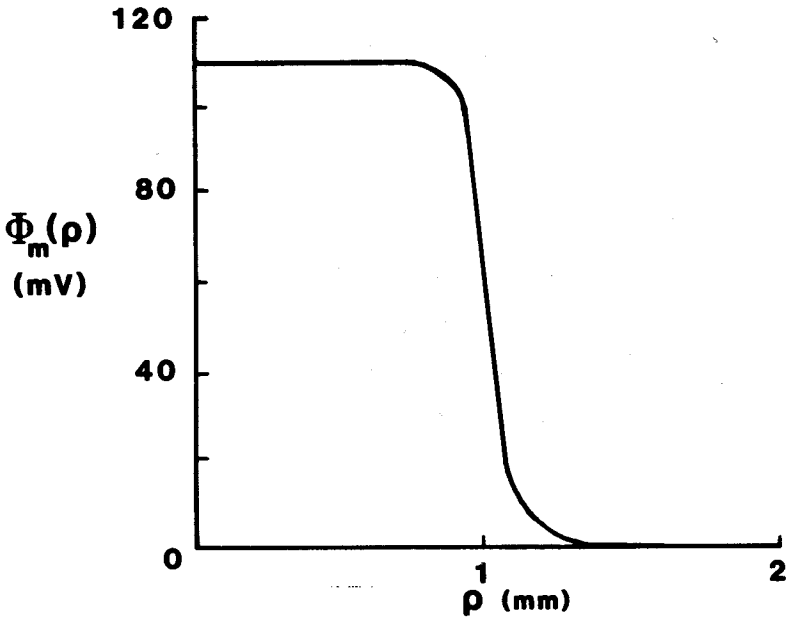

FIG. 4. The transmembrane potential used in all our computations, calculated from Equation (28) with $V_{pk} = 110$ mV, $\dot{V}_{max} = 200$ V/s, $u = 0.3$ m/s, and $\rho_0 = 1$ mm.

on the order of $uV_{pk}/\dot{V}_{max}$, which in our case is 0.17 mm. We describe the electrical properties of the tissue parallel and transverse to the local fiber direction by using the intracellular and interstitial conductivities measured by Clerc [35]: $\sigma_{il} = 0.17$, $\sigma_{ol} = 0.62$, $\sigma_{it} = 0.019$, and $\sigma_{ot} = 0.24$ S/m. The components of the conductivity tensors can be calculated from Clerc's data and the angle χ between the ρ-direction and the fiber direction, using Eq. (3). We assume that the tissue has a thickness l of 1 mm.

Figure 5 illustrates the current and magnetic-field lines produced by the action potential. In Figure 5(a), the current lines (dark bands) and magnetic-field lines (light bands) are those that would exist if there were no electrically silent components of the magnetic field, i.e. if the conductivity tensors were diagonal. The azimuthal component of the current due to the off-diagonal components of the conductivity tensors is shown in Figure 5(b), along with the resulting electrically silent components of the magnetic field. To a first approximation, this is just the magnetic field of a circular current loop of radius ρ_0. Figure 5(c), (d), and (e) show the field lines for the total magnetic field, which is the sum of both the silent and nonsilent components. In Figure 5(c) the electrically detectable components are much smaller than the silent components, while in Figure 5(d) and (e) the electrically

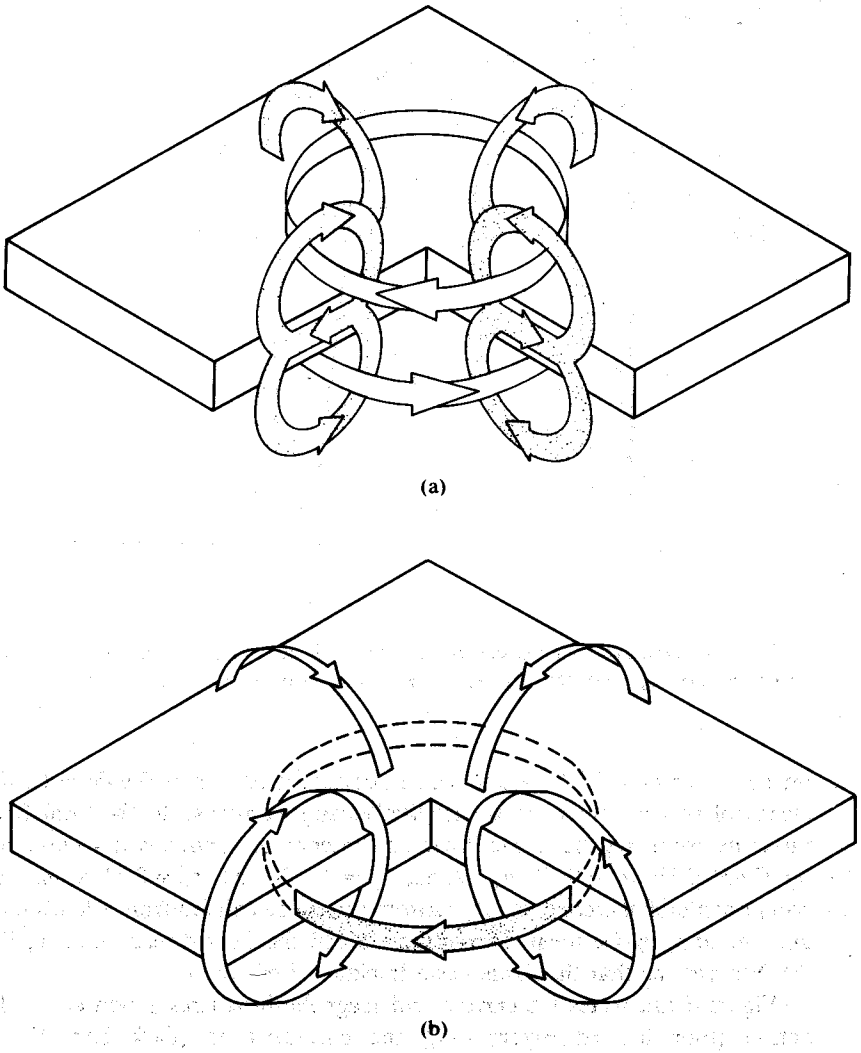

FIG. 5. (a) The current (dark bands) and magnetic-field (light bands) lines created by an action potential propagating outward from the apex of the heart if no off-diagonal terms are present in the conductivity tensors. (b) The azimuthal component of the current and the electrically silent components of the magnetic field produced by off-diagonal terms in the conductivity tensor. (c), (d), (e) The total magnetic field at the apex of the heart, for three cases in which the contribution of the electrically detectable component of the magnetic field is made increasingly larger. This figure is only qualitatively correct; the field lines may not be quantitatively accurate.

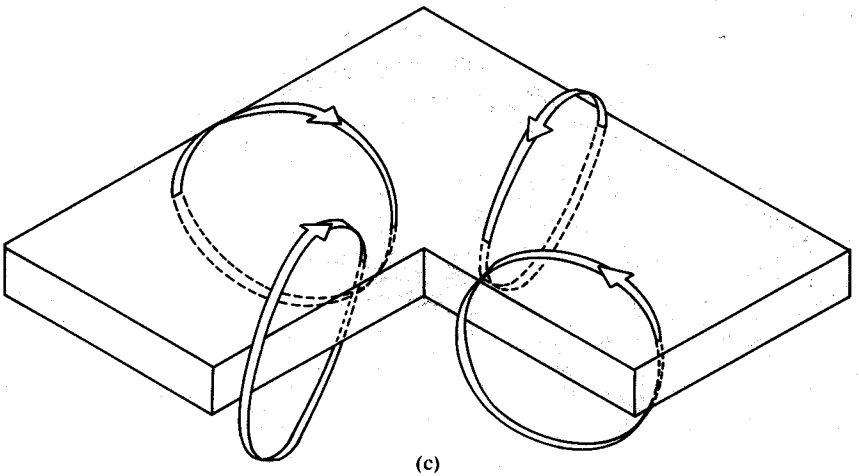

(c)

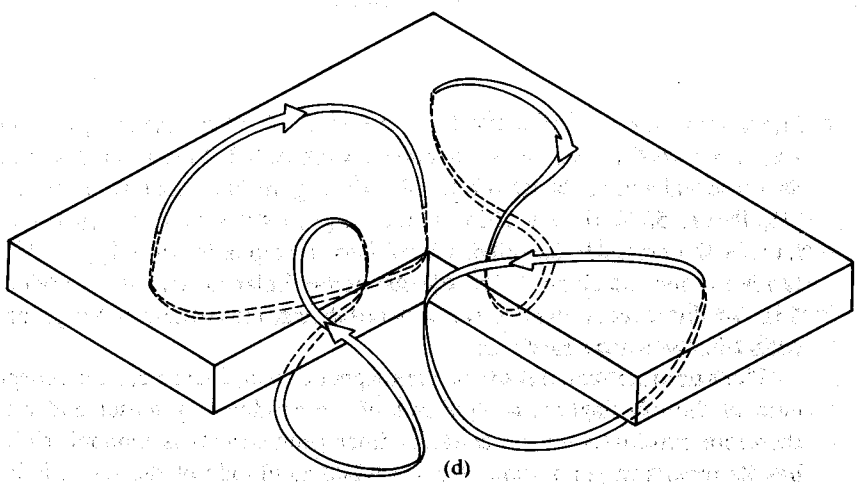

(d)

FIG. 5. Continued.

detectable components are made progressively larger. Figure 5(e) is particularly interesting because the magnetic field lines spiral into the apex in much the same way as do the fibers themselves. We stress that all the drawings in Figure 5 are qualitative and are intended as an aid in developing intuition. They are not quantitatively accurate.

The calculated extracellular potential and the axial (z), radial (ρ), and azimuthal (θ) components of the magnetic field are shown as functions of ρ

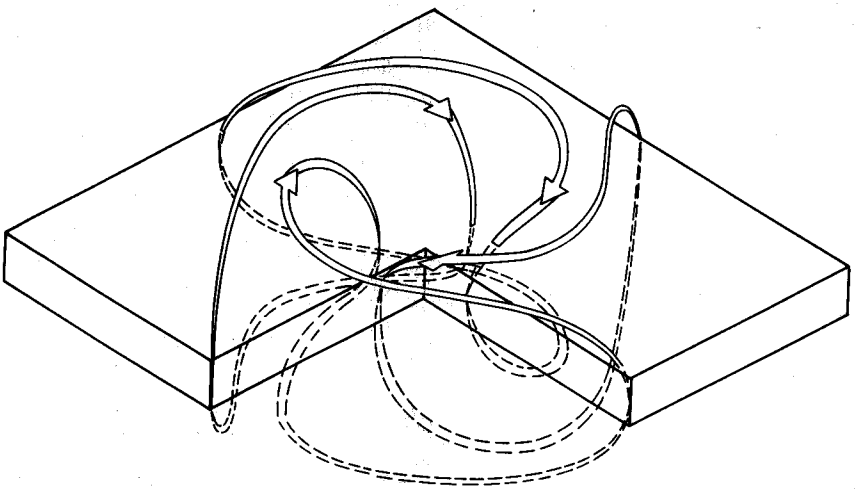

(e)

FIG. 5. Continued.

in Figure 6, for $z = l/2 = 0.5$ mm (on the surface of the tissue), $\rho_0 = 1$ mm, and $\chi = 45°$. Our calculated extracellular potential, Figure 6(a), is similar to those calculated by Spach et al. [10, Figure 8(a)] and Roberge et al. [36, Figure 5(a)]. As the action potential propagates outward (ρ_0 becomes larger), the extracellular potential will become biphasic, with $\Phi_e(\rho = 0) = 0$. Unlike other calculations [10,36], our extracellular potentials are independent of the direction, since we are considering only radial propagation in cylindrically symmetric tissue.

The azimuthal component of the magnetic field, Figure 6(b), is independent of the off-diagonal components of the conductivity tensor and would therefore exist without the spiraling fiber geometry. It is monophasic and has its maximum amplitude at $\rho \approx \rho_0$. The amplitude of the signal is large (≈ 3 nT) compared to most measured biomagnetic signals, since we calculate B^θ at the surface of the tissue, $z = l/2$. The radial and axial components of the magnetic field depend on the off-diagonal terms of the conductivity tensor. The electrically silent radial component, Figure 6(c), has a shape that is similar to the azimuthal component, with a maximum at $\rho \approx \rho_0$. The amplitude of B^ρ is 79% as large as B^θ. Clearly the electrically silent components of **B** are not small perturbations on a signal that otherwise is electrically detectable. The axial component, Figure 6(d), is a biphasic signal, with its maximum amplitude at $\rho \approx 0$ and a second phase that is much smaller in amplitude than the first. The amplitude of B^z is 58% of B^θ. The z

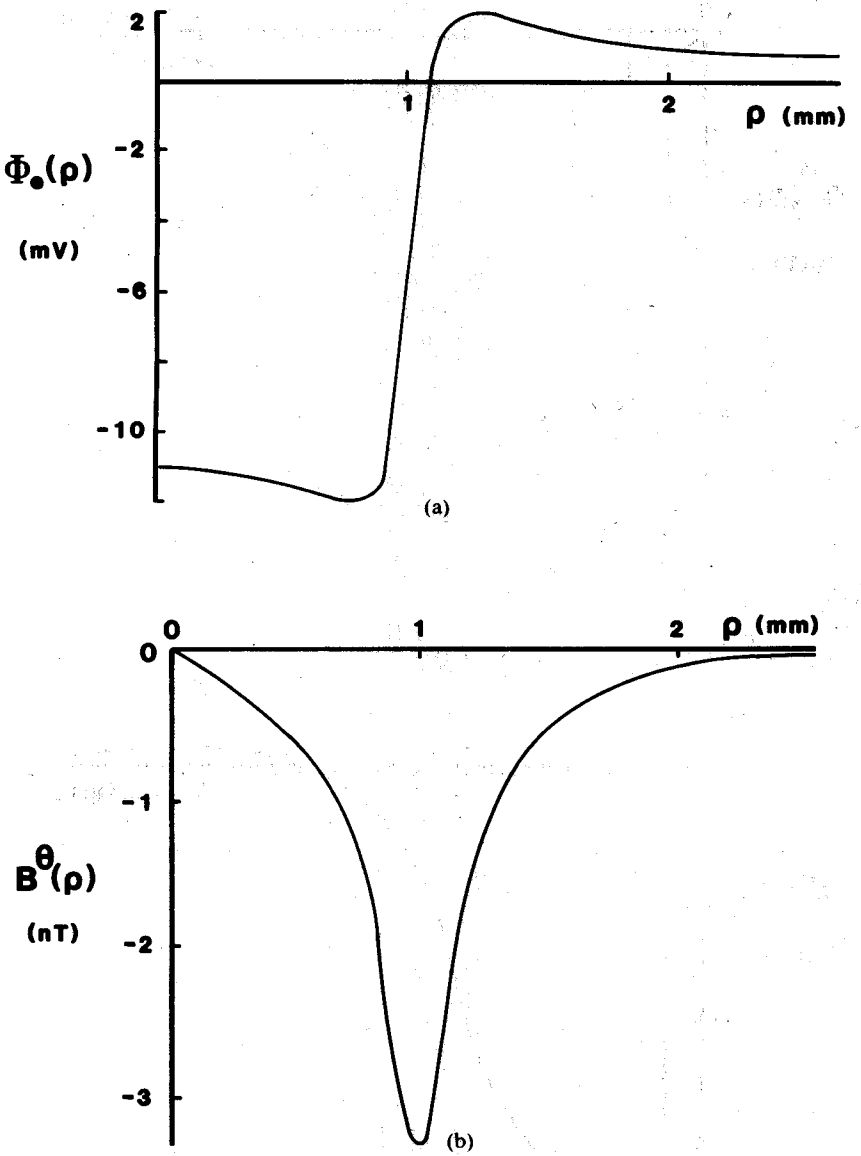

FIG. 6. The (a) external potential, and the (b) azimuthal, (c) radial, and (d) axial components of the magnetic field, calculated for $z = 0.5$ mm, $\chi = 45°$, and $\rho_0 = 1$ mm.

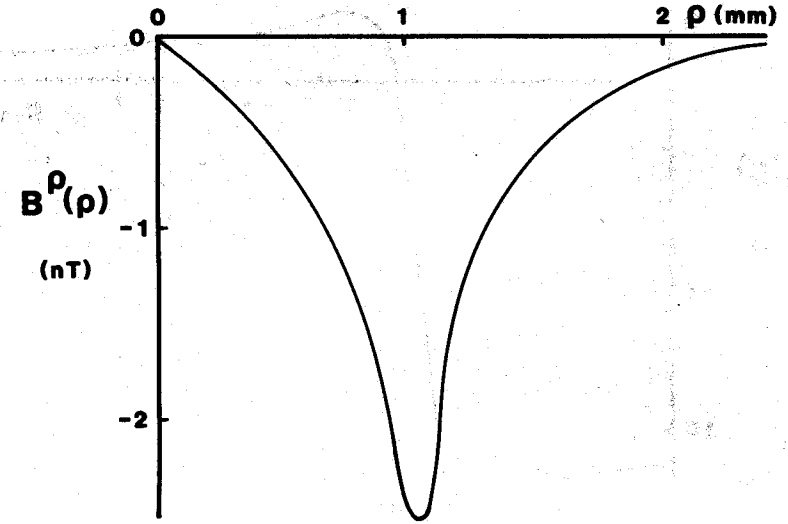

(c)

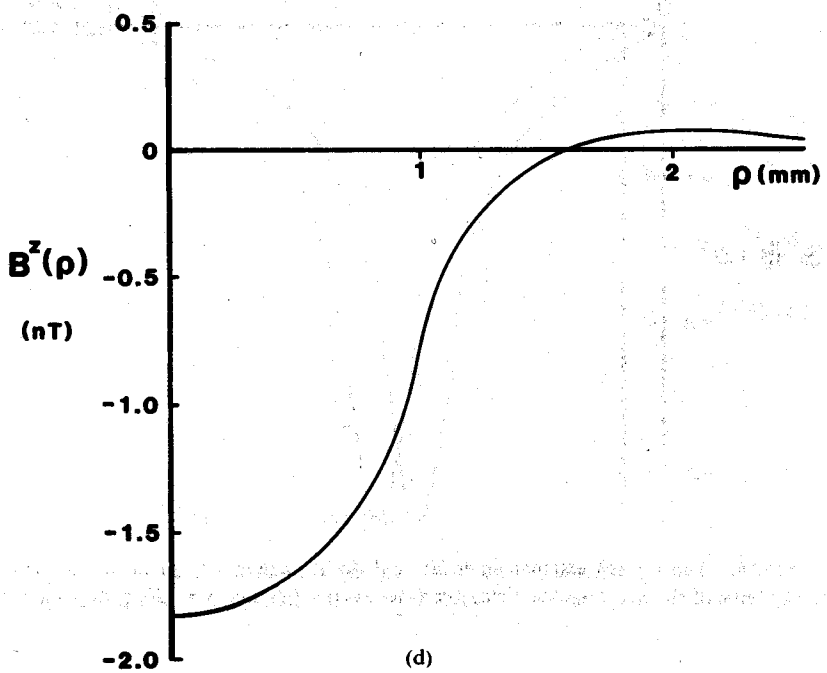

(d)

FIG. 6. Continued.

and ρ components of the magnetic field are similar to those produced by a uniform ring of current of radius ρ_0. In fact, the analytic expression for the magnetic field due to a ring of current is similar to the expressions we have derived [37, Problem 5.4].

Figure 7 shows the amplitude of the three components of the magnetic field as a function of z. Note that the axial component falls off more slowly than the radial or azimuthal components, so that at $z = 2$ mm B^z has nearly twice the amplitude of B^θ or B^ρ. Far from the tissue (where the distance from the field point to the tissue is much larger than ρ_0) only the lowest-order term in a multipole expansion of the magnetic field will be important. Due to the cylindrical symmetry, the magnetic moment of this current distribution must lie in the z-direction. It is produced by the θ-component of the current density, and goes to zero if the conductivity tensors are diagonal. Thus, the magnetic moment generates a dipole magnetic field that is electrically silent. Far from the tissue, the electrically silent dipole field completely

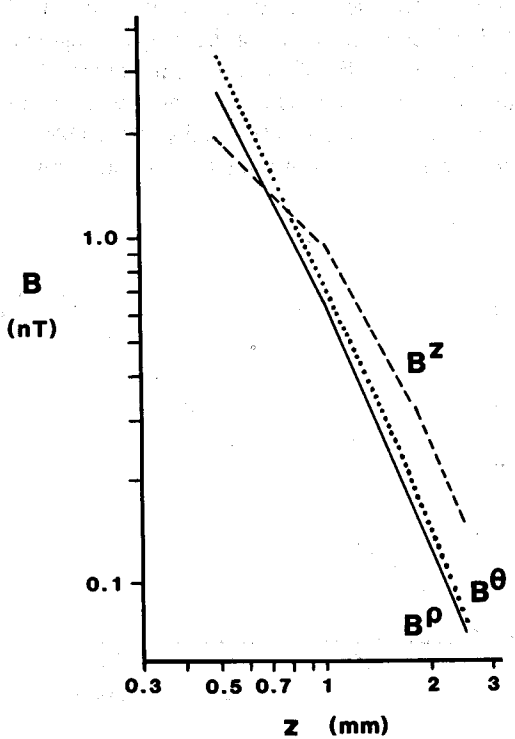

FIG. 7. The peak amplitude of the azimuthal (θ), radial (ρ), and axial (z) components of the magnetic field as a function of z, calculated for $\chi = 45°$ and $\rho_0 = 1$ mm.

dominates the higher-order contributions from sources that are electrically detectable. This surprising result is due to the cylindrical symmetry of our model. If the action-potential propagation is not cylindrically symmetric (for instance, if in one direction the action potential fails to propagate because it reaches the edge of the tissue), then sources that are electrically detectable also produce a magnetic moment. Nevertheless, for our cylindrically symmetric case, when the magnetic field is measured far from the tissue, only the electrically silent components will be detected.

As the angle χ between the radial and local fiber directions goes to zero or 90°, the conductivity tensor becomes diagonal, so B^z and B^ρ go to zero. We can now ask for what χ it will be easiest to detect the electrically silent components of the magnetic field, and therefore extract new information. Figure 8 shows a plot of the ratio of the amplitude of the axial and the azimuthal components of the magnetic field versus χ. The curve reaches a maximum at about 70°, at which angle $B^z/B^\theta \approx 0.6$. Note that the maximum in this curve is not sharp, indicating that there is a wide range of χ-values that will produce large electrically silent components of the magnetic field. From Figure 1, χ is approximately 40°. The amplitude of the magnetic field will also depend on radius of the propagating action potential, ρ_0. Figure 9 shows the ratio B^z/B^θ at different values of ρ_0. The ratio reaches a maximum at $\rho_0 \approx 1$ mm. Thus the relative contributions of the terms that are electrically silent and electrically detectable change as the action potential propagates away from the site of stimulation.

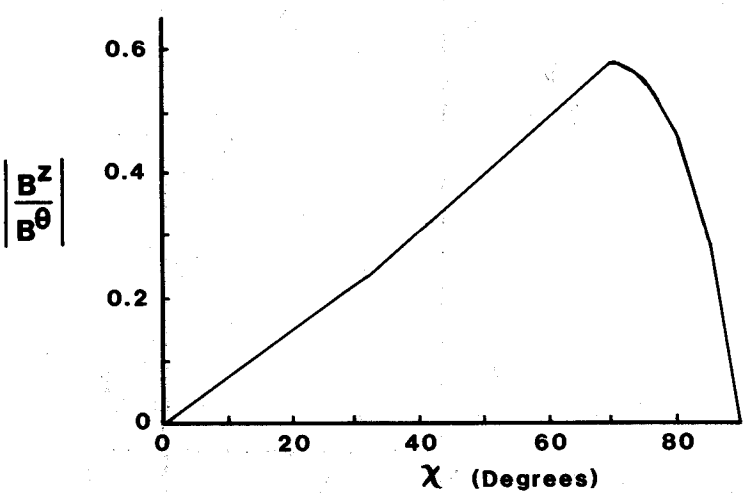

FIG. 8. The ratio of the amplitude of the axial component of the magnetic field to the amplitude of the azimuthal component as a function of χ, the angle between the radial and local fiber directions.

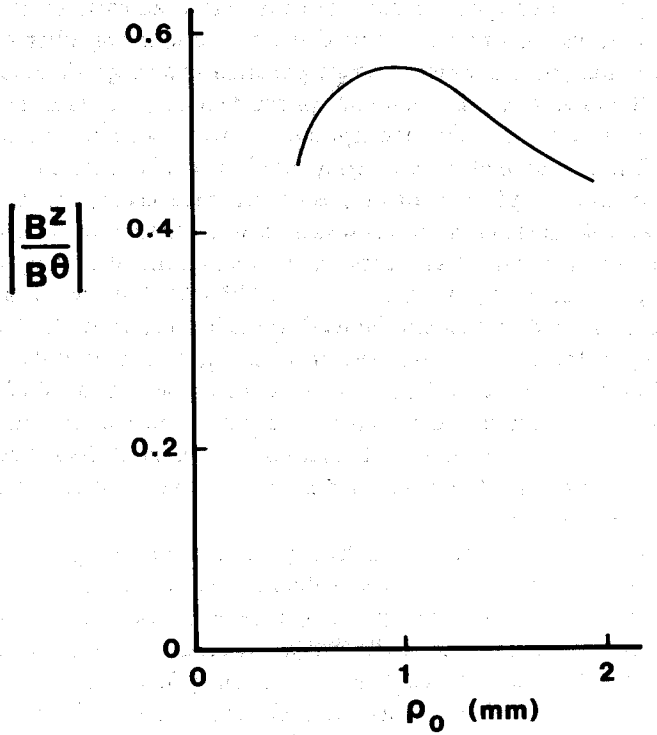

FIG. 9. The ratio of the amplitude of the axial component of the magnetic field to the amplitude of the azimuthal component as a function of ρ_0, the radius of the radially propagating transmembrane potential, calculated for $z = 0.5$ mm and $\chi = 45°$.

DISCUSSION

The magnetic field of a propagating action potential can in principle contain information about cardiac tissue that is not obtainable from measurements of the intracellular and extracellular action potentials. With certain tissue geometries, the magnetic field is affected by components of the current that are electrically silent. In this analysis these currents depend on the off-diagonal components of the conductivity tensors, whereas the electrically detectable currents are determined solely by the diagonal components. Hence the magnetic field is determined by all elements of the conductivity tensors, whereas the electric field is determined only by the diagonal elements. If the off-diagonal terms affect the distribution of action currents, then these effects will be manifested in the magnetic field but not in the electric potential.

This paper extends our analytic treatment of an anisotropic bidomain to two-dimensional propagation in tissue with a spiraling fiber geometry. To obtain analytic expressions for the potential and magnetic field, we require that the local fiber direction make a constant angle χ with the ρ-direction. This is a very restrictive assumption, and will not in general be valid. The justification for making this assumption is that it leads to a conductivity tensor that is independent of position (homogeneous) when expressed in cylindrical coordinates. Fibers which make a constant angle with the radial direction trace out a logarithmic spiral, first discussed by Descartes in 1638 [38], and defined by the equation $\rho = e^{\theta \cot \chi}$ [39]. The curve is asymptotic at the origin, so that it cannot be used to model accurately the fiber geometry exactly at the apex, $\rho = 0$. However, when ρ_0, the radius of the wavefront, is much larger than $uV_{pk}/\dot{V}_{max}$, the width of the wavefront (0.17 mm for our parameters), then the largest currents occur within the depolarization wavefront. If we pick χ so that it matches the observed fiber direction in the depolarization front, the behavior of the fibers at $\rho = 0$ should not seriously affect our calculations.

As is always the case in electrophysiological modeling, the homogeneous problem can be solved easily, but the inhomogeneous problem better represents the biological tissue, in which case χ is not constant, so $\tilde{\sigma}_i$ and $\tilde{\sigma}_o$ depend on ρ, θ, and z. Although introduction of an inhomogeneous conductivity would probably make an analytic solution to the problem impossible, numerical techniques such as finite-element calculations can handle the inhomogeneous problem [17,40,41]. These numerical techniques would be well suited for the extension of this analysis to three-dimensional wavefronts in the whole heart. There exist accurate descriptions of the fiber geometry [27] and propagation path [25] in the human heart, and it may be that numerical calculations based on ideas presented here could accurately model the human ECG and MCG.

It is the spiraling fiber geometry that leads to electrically silent magnetic fields, and in this particular case we expressed that fiber geometry mathematically using off-diagonal terms in the conductivity tensors. However, the conductivity tensors may or may not be diagonal, depending on the coordinate system in which they are expressed. A parallel and uniform fiber geometry (as assumed by Spach et al. [10], Plonsey and Barr [33], and Sepulveda and Wikswo [17]), gives rise to a conductivity tensor that is not diagonal when expressed in cylindrical coordinates, but this fiber geometry does not give rise to electrically silent magnetic fields. While no truly new information is present in the magnetic field in this restrictive geometry, Sepulveda and Wikswo [17] show that the electric and magnetic fields have different sensitivities to each diagonal component of the intracellular and extracellular conductivity tensors and that combined electric and magnetic measurements of the activation potentials and currents may be required for

unique determination of these conductivities. It is the spiraling or helical fiber geometry that is crucial for producing new information in the magnetic field. Thus, it is not surprising that recent experiments using one-dimensional strands of cardiac tissue [18,42,43] did not find new information in the magnetic field, since these investigators intentionally used preparations having uniform fiber geometries.

Based on our study of the electric and magnetic fields produced by a nerve axon [44,45], it should be possible to extend the present analysis to solve the inverse problem of determining the conductivity tensors from combined measurements of the electric and magnetic fields. In principle the four-electrode technique for impedance measurement could also be used to determine the conductivity tensors, since for a small patch of tissue the tensors are diagonal when expressed in a coordinate system aligned with the local fiber axis. However, this would require using electrode separations that are small relative to the distance over which the local fiber direction significantly changes, which is on the order of a millimeter. To separate the intracellular and interstitial conductivities would require using several electrode spacings [46], and four-electrode measurements in an anisotropic bidomain have only been theoretically analyzed for the restrictive case of tissue in the steady state with equal anisotropy ratios [46]. Thus, combined electric and magnetic measurements may provide a valuable alternative to the four-electrode technique for determining the properties of cardiac tissue with spiraling fiber geometry.

What is the significance of this model of the apex of the heart in light of the controversy over the relative information content of the ECG and MCG? First, this model, along with that in Reference [1], demonstrate that electrically silent magnetic fields can be produced by tissues with spiraling or helical fiber geometries. It provides a mechanism for producing current loops like those hypothesized by Wikswo and Barach [6]. Perhaps the most important aspect of this model is that it can be verified experimentally, providing an unambiguous test for the presence of new information in biomagnetic fields. In addition, measurement of the electrically silent magnetic field near exposed cardiac tissue provides a unique means to determine the off-diagonal elements of the tissue conductivity tensors and to assess the effect that the fiber geometry producing these terms has on cardiac activation. Once this model is confirmed experimentally, the question will no longer be whether new information *can* exist in the biomagnetic field, but instead whether it *does* exist in the MCG of the normal or pathological heart. This question is much more difficult to answer, since the fiber geometry [27] and path of the depolarization wavefront [25] are much more complex in the intact human heart, and the MCG is typically recorded at the surface of the chest, several centimeters from the heart. The fact that electrically silent and electrically detectable magnetic fields exhibit different

falloff with distance and very different field patterns might be an important factor to consider in the magnetic localization of ectopic foci and other aberrant electrical activity propagating outward from highly localized activation sites.

APPENDIX A. DERIVATION OF THE EQUATIONS FOR THE ELECTRIC POTENTIAL

In this appendix we will derive expressions for the potentials Φ_i, Φ_o, and Φ_e in terms of the transmembrane potential Φ_m. We can express the transmembrane potential as an expansion of J_0 Bessel functions for different values of the spatial frequency k:

$$\Phi_m(\rho) = \int_0^\infty \phi_m(k) J_0(k\rho)\, dk. \tag{A1}$$

We can use the orthogonality of Bessel functions [37] to invert Equation (A1), finding that

$$\phi_m(k) = k\int_0^\infty \Phi_m(\rho) J_0(k\rho)\, \rho\, d\rho. \tag{A2}$$

Since $\Psi(\lambda z, \rho)$ and $\Phi_e(z, \rho)$ both are solutions to Laplace's equation, we can write them as expansions in terms of the eigenfunctions of Laplace's equation in a cylindrical coordinate system, i.e. Bessel functions in ρ and exponentials in z. Using the relationships between exponential and hyperbolic functions, symmetry arguments, and constraints on the behavior of the potential at the origin, we find the expansions reduce to

$$\Psi(z, \rho) = \int_0^\infty A(k) J_0(k\rho) \cosh(\lambda k z)\, dk, \qquad -l/2 < z < l/2, \tag{A3}$$

$$\Phi_e(z, \rho) = \begin{cases} \int_0^\infty B(k) J_0(k\rho) e^{-kz}\, dk, & z > l/2, \\ \int_0^\infty B(k) J_0(k\rho) e^{kz}\, dk, & z < -l/2, \end{cases} \tag{A4}$$

where $A(k)$ and $B(k)$ are unknown functions to be determined by the boundary conditions and λ is defined in Equation (17). We will find it useful to define the Fourier transforms $\psi(z, k)$, $\phi_e(z, k)$, $\phi_i(z, k)$, and $\phi_o(z, k)$ in the same way as we defined $\phi_m(k)$ in Eq. (A1). Thus, from Eqs. (A3) and (A4) we find that

$$\psi(z, k) = A(k) \cosh(\lambda k z), \qquad -l/2 < z < l/2, \tag{A5}$$

and

$$\phi_e(z, k) = \begin{cases} B(k) e^{-kz}, & z > l/2, \\ B(k) e^{kz}, & z < -l/2. \end{cases} \tag{A6}$$

After applying the boundary conditions given in Eqs. (23) and (24) and doing some algebra, we find that ψ and ϕ_e can be expressed in terms of ϕ_m as

$$\psi(z,k) = \frac{\cosh(\lambda kz)}{\cosh(\lambda kl/2)\,\beta(\lambda,k,l)}\phi_m(k), \qquad -l/2 < z < l/2, \quad \text{(A7)}$$

and

$$\phi_e(z,k) = \begin{cases} -\dfrac{e^{-kz}}{e^{-kl/2}\alpha(k,\lambda,l)}\phi_m(k), & z > l/2, \\ -\dfrac{e^{kz}}{e^{-kl/2}\alpha(k,\lambda,l)}\phi_m(k) & z < -l/2, \end{cases} \quad \text{(A8)}$$

where

$$\alpha(k,\lambda,l) = \frac{\sigma_i^{\rho\rho} + \sigma_o^{\rho\rho}}{\sigma_i^{\rho\rho}} + \gamma(k,\lambda,l), \quad \text{(A9)}$$

$$\beta(k,\lambda,l) = 1 + \frac{\sigma_i^{\rho\rho} + \sigma_o^{\rho\rho}}{\sigma_i^{\rho\rho}} \frac{1}{\gamma(k,\lambda,l)}, \quad \text{(A10)}$$

and

$$\gamma(k,\lambda,l) = \lambda \frac{\sigma_e}{\sigma_i^{\rho\rho}} \frac{\cosh(\lambda kl/2)}{\sinh(\lambda kl/2)}. \quad \text{(A11)}$$

We can now solve for ϕ_i and ϕ_o using Equations (20) and (21):

$$\phi_o(z,k) = \frac{\sigma_i^{\rho\rho}}{\sigma_i^{\rho\rho} + \sigma_o^{\rho\rho}} \left[\frac{\cosh(\lambda kz)}{\cosh(\lambda kl/2)\,\beta(k,\lambda,l)} - 1 \right] \phi_m(k), \quad \text{(A12)}$$

$$\phi_i(z,k) = \frac{\sigma_i^{\rho\rho}}{\sigma_i^{\rho\rho} + \sigma_o^{\rho\rho}} \left[\frac{\cosh(\lambda kz)}{\cosh(\lambda kl/2)\,\beta(k,\lambda,l)} + \frac{\sigma_o^{\rho\rho}}{\sigma_i^{\rho\rho}} \right] \phi_m(k). \quad \text{(A13)}$$

Equations (A8), (A12), and (A13) provide our final result, the potential in each domain in terms of the transmembrane potential.

APPENDIX B. DERIVATION OF THE EQUATIONS FOR THE MAGNETIC FIELD

The magnetic field is calculated from the current density using the law of Biot and Savart, which can be written as [45]

$$\mathbf{B}(\mathbf{r}) = \frac{\mu_0}{4\pi} \left(\int_s \frac{\mathbf{J} \times \mathbf{n}}{|\mathbf{r} - \mathbf{r}'|}\, dS + \int_v \frac{\nabla \times \mathbf{J}}{|\mathbf{r} - \mathbf{r}'|}\, dV \right). \quad \text{(B1)}$$

There are two terms in the equation, a surface (s) and a volume (v) integral. However, there are three components to the magnetic field in the radial (ρ), azimuthal (θ), and axial (z) directions, and three regions over which to integrate, intracellular (i), interstitial (o), and external (e), so that there are actually eighteen separate integrals to evaluate. Seven of these integrals vanish, so there are only eleven left, listed in Table 1. We outline the steps required to evaluate two of these integrals; the rest follow analogously.

As our example, we will integrate the cross product of the current density and the surface normal in the intracellular volume over the surfaces $z = \pm l/2$, calculating the magnetic field at a point outside the tissue, $z > l/2$. We let $\theta = 0$, which leads to no loss of generality, since the fields are all cylindrically symmetric. The unit normal to the surface $z = l/2$ is $\mathbf{z}$. It follows that

$$\mathbf{J}_i \times \mathbf{n} = \left(\sigma_i^{\rho\rho}\boldsymbol{\theta} - \sigma_i^{\theta\rho}\boldsymbol{\rho}\right)\frac{\partial \Phi_i}{\partial \rho}. \tag{B2}$$

Using the fact that the derivative of J_0 is $-J_1$, we can express $\partial\Phi_i/\partial\rho$ as

$$\frac{\partial \Phi_i}{\partial \rho} = -\int_0^\infty \phi_i(z, w)\, w J_1(w\rho)\, dw. \tag{B3}$$

The function $1/|\mathbf{r}-\mathbf{r}'|$ can be rewritten in terms of trigonometric functions in θ, Bessel functions in ρ, and exponential functions in z, as [37, Problem 3.14]

$$\frac{1}{|\mathbf{r}-\mathbf{r}'|} = \int_0^\infty dk\, e^{-k(z_> - z_<)} \times \left[J_0(k\rho)J_0(k\rho') - 2\sum_{m=1}^{\infty} \cos m\theta' J_m(k\rho)J_m(k\rho')\right], \tag{B4}$$

where $z_>$ and $z_<$ are the larger and smaller of the two variables z and z'. In our case, $z_< = l/2$ and $z_> = z$. Combining Equations (B2), (B3), and (B4), we can rewrite the surface integral in Equation (B1) as

$$\begin{aligned} B_{i,s}(z,\rho) &= \frac{\mu_0}{4\pi}\int_0^\infty \int_0^{2\pi} \left\{\left(\sigma_i^{\theta\rho}\rho' - \sigma_i^{\rho\rho}\theta'\right)\int_0^\infty \phi_i(l/2, w)\, w J_1(w\rho')\, dw\right\} \\ &\times \left\{\int_0^\infty e^{-kz} e^{kl/2}\left[J_0(k\rho)J_0(k\rho') - 2\sum_{m=1}^{\infty}\cos m\theta' J_m(k\rho)J_m(k\rho')\right] dk\right\} \\ &\times \rho'\, d\rho'\, d\theta'. \end{aligned} \tag{B5}$$

TABLE 1

$$B^{\rho}_{i,s}(z,\rho) = \mu_0 \frac{\sigma_i^{\rho\rho}}{\sigma_i^{\rho\rho}+\sigma_o^{\rho\rho}} \sigma_i^{\theta\rho} \int_0^{\infty} dk \left[\frac{1}{\beta(k,\lambda,l)} + \frac{\sigma_o^{\rho\rho}}{\sigma_i^{\rho\rho}} \right] \sinh\left(\frac{kl}{2}\right) \phi_m(k) J_1(k\rho) e^{-kz}, \quad \text{(B11)}$$

$$B^{\theta}_{i,s}(z,\rho) = -\mu_0 \frac{\sigma_i^{\rho\rho}}{\sigma_i^{\rho\rho}+\sigma_o^{\rho\rho}} \sigma_i^{\rho\rho} \int_0^{\infty} dk \left[\frac{1}{\beta(k,\lambda,l)} + \frac{\sigma_o^{\rho\rho}}{\sigma_i^{\rho\rho}} \right] \sinh\left(\frac{kl}{2}\right) \phi_m(k) J_1(k\rho) e^{-kz}, \quad \text{(B12)}$$

$$B^{\rho}_{i,v}(z,\rho) = -\mu_0 \frac{\lambda^2}{1-\lambda^2} \frac{\sigma_i^{\rho\rho}}{\sigma_i^{\rho\rho}+\sigma_o^{\rho\rho}} \sigma_i^{\theta\rho} \int_0^{\infty} dk \frac{1}{\beta(k,\lambda,l)} \sinh\left(\frac{kl}{2}\right)$$
$$\times \left[\frac{\sinh(k\lambda l/2)\cosh(kl/2)}{\lambda \sinh(kl/2)\cosh(k\lambda l/2)} - 1 \right] \phi_m(k) J_1(k\rho) e^{-kz}, \quad \text{(B13)}$$

$$B^{\theta}_{i,v}(z,\rho) = -\mu_0 \frac{\lambda^2}{1-\lambda^2} \frac{\sigma_i^{\rho\rho}}{\sigma_i^{\rho\rho}+\sigma_o^{\rho\rho}} (\sigma_i^{zz} - \sigma_i^{\rho\rho})$$
$$\times \int_0^{\infty} dk \frac{1}{\beta(k,\lambda,l)} \sinh\left(\frac{kl}{2}\right) \left[\frac{\sinh(k\lambda l/2)\cosh(kl/2)}{\lambda \sinh(kl/2)\cosh(k\lambda l/2)} - 1 \right]$$
$$\times \phi_m(k) J_1(k\rho) e^{-kz}, \quad \text{(B14)}$$

$$B^{z}_{i,v}(z,\rho) = \mu_0 \frac{1}{1-\lambda^2} \frac{\sigma_i^{\rho\rho}}{\sigma_i^{\rho\rho}+\sigma_o^{\rho\rho}} \sigma_i^{\theta\rho}$$
$$\times \int_0^{\infty} dk \left\{ \frac{1}{\beta(k,\lambda,l)} \left[1 - \frac{\lambda \cosh(kl/2)\sinh(k\lambda l/2)}{\sinh(kl/2)\cosh(k\lambda l/2)} \right] + \frac{\sigma_o^{\rho\rho}}{\sigma_i^{\rho\rho}} \frac{(1-\lambda^2)}{\cosh(\lambda k l/2)} \right\}$$
$$\times \sinh\left(\frac{kl}{2}\right) \phi_m(k) J_0(k\rho) e^{-kz}, \quad \text{(B15)}$$

$$B^{\rho}_{o,s}(z,\rho) = \mu_0 \frac{\sigma_i^{\rho\rho}}{\sigma_i^{\rho\rho}+\sigma_o^{\rho\rho}} \sigma_o^{\theta\rho} \int_0^{\infty} dk \left[\frac{1}{\beta(k,\lambda,l)} - 1 \right] \phi_m(k) \sinh\left(\frac{kl}{2}\right) J_1(k\rho) e^{-kz}, \quad \text{(B16)}$$

$$B^{\theta}_{o,s}(z,\rho) = -\mu_0 \frac{\sigma_i^{\rho\rho}}{\sigma_i^{\rho\rho}+\sigma_o^{\rho\rho}} \sigma_o^{\rho\rho} \int_0^{\infty} dk \left[\frac{1}{\beta(k,\lambda,l)} - 1 \right] \phi_m(k) \sinh\left(\frac{kl}{2}\right) J_1(k\rho) e^{-kz}, \quad \text{(B17)}$$

$$B^{\rho}_{o,v}(z,\rho) = -\mu_0 \frac{\lambda^2}{1-\lambda^2} \frac{\sigma_i^{\rho\rho}}{\sigma_i^{\rho\rho}+\sigma_o^{\rho\rho}} \sigma_o^{\theta\rho} \int_0^{\infty} dk \frac{1}{\beta(k,\lambda,l)} \phi_m(k) \sinh\left(\frac{kl}{2}\right)$$
$$\times \left[\frac{\cosh(kl/2)\sinh(k\lambda l/2)}{\lambda \sinh(kl/2)\cosh(k\lambda l/2)} - 1 \right] J_1(k\rho) e^{-kz}, \quad \text{(B18)}$$

$$B^{\theta}_{o,v}(z,\rho) = -\mu_0 \frac{\lambda^2}{1-\lambda^2} \frac{\sigma_i^{\rho\rho}}{\sigma_i^{\rho\rho}+\sigma_o^{\rho\rho}} (\sigma_o^{zz} - \sigma_o^{\rho\rho})$$
$$\times \int_0^{\infty} dk \frac{1}{\beta(k,\lambda,l)} \left[\frac{\cosh(kl/2)\sinh(k\lambda l/2)}{\lambda \sinh(kl/2)\cosh(k\lambda l/2)} - 1 \right]$$
$$\times \sinh\left(\frac{kl}{2}\right) \phi_m(k) J_1(k\rho) e^{-kz}, \quad \text{(B19)}$$

$$B^{z}_{o,v}(z,\rho) = \mu_0 \frac{1}{1-\lambda^2} \frac{\sigma_i^{\rho\rho}}{\sigma_i^{\rho\rho}+\sigma_o^{\rho\rho}} \sigma_o^{\theta\rho}$$
$$\times \int_0^{\infty} dk \left\{ \frac{1}{\beta(k,\lambda,l)} \left[1 - \frac{\lambda \cosh(kl/2)\sinh(k\lambda l/2)}{\sinh(kl/2)\cosh(k\lambda l/2)} \right] - \frac{1-\lambda^2}{\cosh(k\lambda l/2)} \right\}$$
$$\times \sinh\left(\frac{kl}{2}\right) \phi_m(k) J_0(k\rho) e^{-kz}, \quad \text{(B20)}$$

$$B^{\theta}_{e,s}(z,\rho) = -\mu_0 \sigma_e \int_0^{\infty} dk \frac{1}{\alpha(k,\lambda,l)} \sinh\left(\frac{kl}{2}\right) \phi_m(k) J_1(k\rho) e^{-kz}. \quad \text{(B21)}$$

The unit vectors $\boldsymbol{\rho}'$ and $\boldsymbol{\theta}'$ can be expressed in terms of the Cartesian unit vectors $\mathbf{x}$ and $\mathbf{y}$ by

$$\boldsymbol{\theta}' = -\mathbf{x}\sin\theta' + \mathbf{y}\cos\theta', \tag{B6}$$

$$\boldsymbol{\rho}' = \mathbf{x}\cos\theta' + \mathbf{y}\sin\theta'. \tag{B7}$$

When we integrate over θ' in Equation (B5), all contributions to $\boldsymbol{\rho}$ and $\boldsymbol{\theta}$ containing $\sin\theta'$ vanish, and the only term in the sum over m which survives is $m=1$. Using these facts and rearranging the order of integration, we find that

$$B_{i,s}(z,\rho) = \tfrac{1}{2}\mu_0\left(\sigma_i^{\theta\rho}\mathbf{x} - \sigma_i^{\rho\rho}\mathbf{y}\right)\int_0^\infty dw \int_0^\infty dk\, \phi_i(l/2, w)\, wJ_1(k\rho)e^{-kz}e^{kl/2}$$

$$\times \int_0^\infty J_1(w\rho')\, J_1(k\rho')\, \rho'\, d\rho'. \tag{B8}$$

We now use the orthogonality relationship [37]

$$\frac{1}{k}\delta(k-w) = \int_0^\infty \rho J_1(k\rho)\, J_1(w\rho)\, d\rho, \tag{B9}$$

to simplify Eq. (B8) to

$$B_{i,s}(z,\rho) = \tfrac{1}{2}\mu_0\left(\sigma_i^{\theta\rho}\mathbf{x} - \sigma_i^{\rho\rho}\mathbf{y}\right)\int_0^\infty dk\, \phi_i(l/2, k)\, J_1(k\rho)e^{kl/2}e^{-kz}. \tag{B10}$$

If we now do the same integral over the surface $z=-l/2$, add the two results, substitute for $\phi_i(l/2,k)$ from Equation (A16), and note that at $\theta=0$, $\mathbf{x}=\boldsymbol{\rho}$, and $\mathbf{y}=\boldsymbol{\theta}$, we get Equations (B11) and (B12) in Table 1.

APPENDIX C. COMPUTATIONAL ASPECTS OF THE CALCULATION

The expressions in appendices A and B all have the general form

$$\int_0^\infty f(z,k)\, \phi_m(k)\, J_{0,1}(k\rho)\, dk, \tag{C1}$$

where $f(z,k)$ depends on exactly which potential or component of the magnetic field is desired. The first step in our calculation is to compute $\phi_m(k)$ from $\Phi_m(\rho)$ using Equation (A2). We can consider this step as a transformation of the transmembrane potential from a function of ρ to a function of k, analogous to a Fourier transformation but using Bessel instead of sinusoidal functions. We call k the spatial frequency, although it is not a frequency in the same sense as it would be in a Fourier transformation. Figure 10(a) shows $\phi_m(k)$ calculated from the transmembrane potential

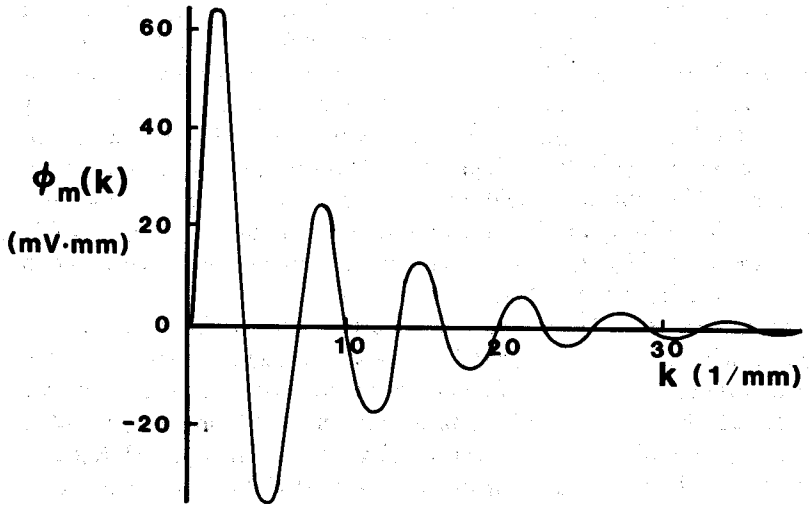

(a)

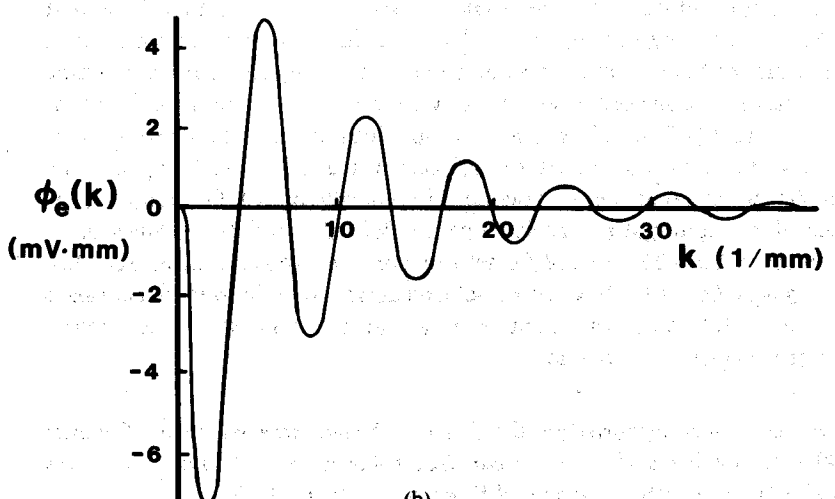

(b)

FIG. 10. The transform of (a) the transmembrane potential and (b) the external potential calculated at $z = 0.5$ mm for $\chi = 45°$ and $\rho_0 = 1$ mm.

that is shown in Figure 4. We next multiply $\phi_m(k)$ by the filter function $f(z,k)$ to arrive at the potential or magnetic field in transform space. In Figure 10(b) we show the transform of the external potential, $\phi_e(z,k)$, at $z=l/2$ obtained by multiplying $\phi_m(k)$ by the filter function defined by Equation (A11). This product is then transformed back into a function of ρ, using an equation analogous to Equation (A1) for the potential and the axial component of the magnetic field, or using an equation like Equation (A1) with J_0 replaced by J_1 for the radial and azimuthal components (see Table 1). For example, Figure 6(a) shows the inverse transform of the function $\phi_e(z,k)$ shown in Figure 10(b).

This procedure is reminiscent of the calculation of the potential and magnetic field of a nerve axon [45]. In that case the transmembrane potential Φ_m was a function of z, while here it is a function of ρ. For the nerve, we transformed $\Phi_m(z)$ to $\phi_m(k)$ using a Fourier transform and the filter functions contained modified Bessel functions such as $I_0(ka)$ and $K_0(k\rho)$, where a was the radius of the axon. For our calculation, we transformed $\Phi_m(\rho)$ to $\phi_m(k)$ using a Bessel-function transform, and the filter functions contained exponential functions such as $\cosh(kl)$ and e^{-kz}, where l is the width of the slab of tissue.

One important difference between the two calculations is that there exist efficient fast-Fourier-transform (FFT) algorithms for performing Fourier transforms, but we know of no analogous "fast" algorithm for computing Bessel-function transforms. Therefore, we calculated the integrals in Equations (A1) and (A2) by discretizing the functions, limiting the range of k or ρ values over which we integrate, and then using a rectangular quadrature algorithm to approximate the integral. We typically used 1000 evenly spaced values of ρ, separated by the increment 0.002 mm, and 1000 values of k, separated by 0.05 mm^{-1}. The Bessel functions were calculated using IMSL routines [47]. One advantage of Bessel transforms over Fourier transforms is that the Bessel transform contains only real numbers, while the Fourier transform is generally complex.

This work was supported by the Office of Naval Research under Contract N00014-82-K-0107 and the American Heart Association. Computer time was provided by the College of Arts and Science, Vanderbilt University.

REFERENCES

1 B. J. Roth and J. P. Wikswo, Jr., Electrically-silent magnetic fields, *Biophys. J.* 50:739–745 (1986).

2 G. M. Baule and R. Mcfee, Detection of the magnetic field of the heart, *Amer. Heart J.* 66:95–96 (1963).

3 D. Cohen, Magnetic fields of the human body, *Phys. Today* 28:34–43 (1975).

4 R. Plonsey, Capability and limitations of electrocardiography and magnetocardiography, *IEEE Trans. Biomed. Engrg.* BME-22:239–244 (1972).
5 S. Rush, On the independence of the magnetic and electric body surface recordings, *IEEE Trans. Biomed. Engrg.* BME-22:157–167 (1975).
6 J. P. Wikswo, Jr., and J. P. Barach, Possible sources of new information in the magnetocardiogram, *J. Theoret. Biol.* 95:721–729 (1982).
7 L. V. Corbin, III and A. M. Scher, The canine heart as an electrocardiographic generator. Dependence on cardiac orientation, *Circ. Res.* 41:58–67 (1977).
8 P. Colli-Franzone, L. Guerri, C. Viganotti, E. Macchi, S. Baruffi, S. Spaggiari, and B. Taccardi, Potential fields generated by oblique dipole layers modeling excitation wavefronts in the anisotropic myocardium, *Circ. Res.* 51:330–346 (1982).
9 P. Colli-Franzone, L. Guerri, B. Taccardi, S. Tentoni, and C. Viganotti, Cardiac fibers orientation and potential fields: Model studies, *Japan. Heart J.* (suppl.) 23:279–281 (1982).
10 M. S. Spach, W. T. Miller, III, E. Miller-Jones, R. B. Warren, and R. C. Barr, Extracellular potentials related to intracellular action potentials during impulse conduction in anisotropic canine cardiac muscle, *Circ. Res.* 45:188–204 (1979).
11 M. S. Spach, W. T. Miller, III, D. B. Geselowitz, R. C. Barr, J. M. Kootsey, and E. A. Johnson, The discontinuous nature of propagation in normal canine cardiac muscle. Evidence for recurrent discontinuities of intracellular resistance that affect the membrane currents, *Circ. Res.* 48:39–54 (1981).
12 T. Katila and P. Karp, Magnetocardiography: Morphology and multipole presentations, in *Biomagnetism: An Interdisciplinary Approach* (S. J. Williamson, G. Romani, L. Kaufman, and I. Modena, Eds.), Plenum, 1983, pp. 237–263.
13 J. P. Wikswo, Jr., Theoretical aspects of the ECG-MCG relationship, in *Biomagnetism: An Interdisciplinary Approach* (S. J. Williamson, G. Romani, L. Kaufman, and I. Modena, Eds.), Plenum, 1983, pp. 311–326.
14 R. Plonsey, The nature of sources of bioelectric and biomagnetic fields, *Biophys. J.* 39:309–312 (1982).
15 L. I. Titomir and P. Kneppo, Simultaneous analysis of the cardiac electric and magnetic fields using the scalar multipole expansion, *Bull. Math. Biol.* 47:123–143 (1985).
16 L. I. Titomir and P. Kneppo, On the possibility to determine integral characteristics of the cardiac electric generator from extracardiac electric and magnetic measurements, *IEEE Trans. Biomed. Engrg.* BME-30:222–226 (1983).
17 N. G. Sepulveda and J. P. Wikswo, Jr., Electric and magnetic fields from two-dimensional anisotropic bisyncytia, *Biophys. J.* 51:557–568 (1986).
18 D. Burstein and D. Cohen, Comparison of magnetic field and electric potential produced by frog heart muscle, *J. Appl. Phys.* 57:2640–2646 (1985).
19 C. E. MacAulay, G. Stroink, and B. M. Horacek, Signal analysis of magnetocardiograms and electrocardiograms to test their independence, in *Biomagnetism: Applications and Theory* (H. Weinberg, G. Stroink, and T. Katila, Eds.), Pergamon, 1985, pp. 115–120.
20 C. E. MacAulay, G. Stroink, and B. M. Horacek, Independent information content in magnetocardiograms, presented at IEEE Engineering in Medicine and Biology Society 8th Annual Conference, Dallas–Fort Worth, Tex., 7–10 Nov. 1986.
21 J. Nousiainen, J. Lekkala, and J. Malmivuo, Statistical analysis of the relationship between VMCG and VECG, in *Biomagnetism: Applications and Theory* (H. Weinberg, G. Stroink, and T. Katila, Eds.), Pergamon, 1985, pp. 170–179.

22 T. Varpula, T. Katila, T. Poutanen, and M. Seppanen, In vivo study of the effect of the secondary currents on the MCG, in *Biomagnetism: Applications and Theory* (H. Weinberg, G. Stroink, and T. Katila, Eds.), Pergamon, 1985, pp. 180–185.

23 R. S. Gonnelli and M. Agnello, Inverse problem solution in cardiomagnetism using a current multipole expansion of the primary sources, *Phys. Med. Biol.* 32:133–142 (1987).

24 J. C. Campos, U. Tachinardi, C. P. Melo, and P. Costa Ribeiro, Depolarization orientation in a multiple dipole model for the direct problem in magnetocardiography, in *Biomagnetism* 1987, *Proceedings of the 6th International Conference on Biomagnetism* (Atsumi, Katila, Kotani, Williamson, and Ueno, Eds.), Tokyo Denki Univ. Press, to appear.

25 D. Durrer, R. Th. van Dam, G. E. Freud, M. J. Janse, F. L. Meijler, and R. C. Arzbaicher, Total excitation of the isolated human heart, *Circulation* 41:899–912 (1970)

26 R. S. Gonnelli and M. Agnello, Simulation of an excitation wavefront spreading through an anisotropic myocardium: An analytical model study of the heart magnetic field during ventricular activation, in *Biomagnetism* 1987, *Proceedings of the 6th International Conference on Biomagnetism* (Atsumi, Katila, Kotani, Williamson, and Ueno, Eds.), Tokyo Denki Univ. Press, to appear.

27 D. Streeter, Gross morphology and fiber geometry of the heart, in *Handbook of Physiology*, *Sec.* 2: *The Cardiovascular System* (Stephen R. Geiger, Ed.), Amer. Physiol. Soc., Bethesda, Md., 1979.

28 L. Tung, A Bi-domain Model for Describing Ischemic Myocardial D-C Potentials, Ph.D. Thesis, Mass. Inst. of Tech., 1978.

29 W. T. Miller, III, and D. B. Geselowitz, Simulations of the electrocardiogram, I. The normal heart, *Circ. Res.* 43:301–315 (1978).

30 R. S. Eisenberg, V. Barcilon, and R. T. Mathias, Electrical properties of spherical syncytia, *Biophys. J.* 25:151–180 (1979).

31 D. B. Geselowitz and W. T. Miller, III, A bidomain model for anisotropic cardiac muscle, *Ann. Biomed. Engrg.* 11:191–206 (1983).

32 B. J. Roth and J. P. Wikswo, Jr., A bi-domain model for the extracellular potential and magnetic field of cardiac tissue, *IEEE Trans. Biomed. Engrg.* BME-33:467–469 (1985).

33 R. Plonsey and R. C. Barr, Current flow patterns in two-dimensional anisotropic bisyncytia with normal and extreme conductivities, *Biophys. J.* 45:557–571 (1984).

34 N. Sperelakis, Origin of the cardiac resting potential, in *Handbook of Physiology*, *Sec.* 2: *The Cardiovascular System* (Stephen R. Geiger, Ed.), Amer. Physiol. Soc., Bethesda, Md., 1979.

35 L. Clerc, Directional differences of impulse spread in trabecular muscle from mammalian heart, *J. Physiol.* 255:335–346 (1976).

36 F. A. Roberge, A. Vinet, and B. Victorri, Reconstruction of propagated electrical activity with a two-dimensional model of anisotropic heart muscle, *Circ. Res.* 58:461–475 (1986).

37 J. Jackson, *Classical Electrodynamics*, Wiley, New York, 1975.

38 The logarithmic spiral, *Amer. Math. Monthly* 25:189–193 (1918).

39 J. D. Lawrence, *A Catalog of Special Plane Curves*, Dover, New York, 1972.

40 J. P. Wikswo, Jr., and N. G. Sepulveda, Current pathways in two-dimensional bisyncytial anisotropic cardiac tissue, *Circulation* (suppl. III) 72:238 (1985).

41 N. G. Sepulveda, D. S. Echt, and J. P. Wikswo, Jr., Finite element model of a two-dimensional cardiac bidomain, in *Proceedings of the 38th Annual Conference of Engineering in Medicine and Biology*, 1985, *p.* 341.

42 J. P. Wikswo, Jr., J. P. Barach, S. C. Gundersen, M. J. McLean, and J. A. Freeman, First measurement of action currents in isolated cardiac Purkinje fibers, *Nuovo Cimento D* 2D:368–378 (1983).

43 J. P. Wikswo, Jr., and B. J. Roth, Magnetic measurement of propagating action potentials in isolated one-dimensional cardiac tissue preparations, in *Biomagnetism: Applications and Theory* (H. Weinberg, B. Stroink, and T. Katila, Eds.), Pergamon, New York, 1985, pp. 121–125.

44 B. J. Roth and J. P. Wikswo, Jr., The magnetic field of a single axon: A comparison of theory and experiment, *Biophys. J.* 48:93–109 (1985).

45 J. K. Woosley, B. J. Roth, and J. P. Wikswo, Jr., The magnetic field of a single axon: A volume conductor model, *Math. Biosci.* 76:1–36 (1985).

46 R. Plonsey and R. C. Barr, The four-electrode resistivity technique as applied to cardiac muscle, *IEEE Trans. Biomed. Engrg.* BME-29:541–546 (1982).

47 *IMSL Library 2*, International and Statistical Libraries, Houston, 1977.

48 F. P. Mall, On the muscular architecture of the ventricles of the human heart, *Amer. J. Anat.* 11:211–266 (1911).